Thiazole Functionalization of Thiosemicarbazone for Cu(II) Complexation: Toward Highly Efficient Anticancer Drugs with Promising Oral Bioavailability

Song-Yu Luo , Chun-Mei Zeng , Ping Xu , Ye Ning , Meng-Lin Dong , Wen-Hua Zhang * , Guangliang Yu *

Posted Date: 19 July 2024

doi: 10.20944/preprints202407.1597.v1

Keywords: Thiosemicarbazone; anticancer drug; copper complex; reactive oxygen species; pharmacokinetics

Article

Thiazole Functionalization of Thiosemicarbazone for Cu(II) Complexation: Toward Highly Efficient Anticancer Drugs with Promising Oral Bioavailability

Song-Yu Luo [1,†], Chun-Mei Zeng [1,†], Ping Xu [2], Ye Ning [1], Meng-Lin Dong [1], Wen-Hua Zhang [1,*] and Guangliang Yu [2,*]

[1] College of Chemistry, Chemical Engineering, and Materials Science, Soochow University, Suzhou 215123, China
[2] Suzhou Degen Bio-medical Co., Ltd., No.1 Huayun Road, Suzhou Industrial Park, Suzhou, 215000 Jiangsu, China
* Correspondence: whzhang@suda.edu.cn (W.-H.Z.); yuguangliang@degrontech.onaliyun.com (G.Y.)
† These authors contributed equally to this work.

Abstract: In this work, we report the synthesis of a new thiosemicarbazone-based drug of N′-(di(pyridin-2-yl)methylene)-4-(thiazol-2-yl)piperazine-1-carbothiohydrazide (H**L**) featuring a thiazole spectator for the efficient coordination with Cu(II) to give [CuCl(**L**)]$_2$ (**1**) and [Cu(NO$_3$)(**L**)]$_2$ (**2**). Both **1** and **2** exhibit dimeric structures ascribed to the presence of di-2-pyridylketone moieties that demonstrate dual functions of chelation and intermolecular bridging. H**L**, **1** and **2** are highly toxic against hepatocellular carcinoma cell lines Hep-G2, PLC/PRF/5, and HuH-7, with half maximal inhibitory concentration (IC_{50}) values as low as 3.26 nmol/mL (H**L**), 2.18 nmol/mL (**1**), and 2.54 × 10^{-5} nmol/mL (**2**) for PLC/PRF/5. While the free ligand H**L** may elicit its anticancer effect via sequestration of bio-relevant metal ions (i.e., Fe^{3+} and Cu^{2+}), **1** and **2** are also capable of generating cytotoxic reactive oxygen species (ROS) to inhibit cancer cell proliferation. Our preliminary pharmacokinetic studies revealed that oral administration (per os, PO) of H**L** has a significantly longer half-life $t_{1/2}$ of 21.61 ± 9.4 h, nearly doubled as compared to that of the intravenous (i.v.) administration of 11.88 ± 1.66 h, certifying H**L** as an effective chemotherapeutic drug via PO administration.

Keywords: thiosemicarbazone; anticancer drug; copper complex; reactive oxygen species; pharmacokinetics

1. Introduction

Thiosemicarbazones (TSCs) are a class of Schiff-base derivatives that exhibit diverse biologically beneficial activities, such as antibacterial, antiviral, and enzyme inhibitory activities [1,2]. Most notably, TSCs have long been reported as a highly promising class of drugs for a broad-spectrum of cancers through a wide range of anticancer mechanisms, such as ribonuclease reductase and topoisomerase II inhibition [3–6]. Other mechanisms include the quick sequestration of cell-proliferative-dependent ions **(i.e., Fe^{3+} and Cu^{2+})** to elicit the anticancer effect [4]. The anticancer effect of TSCs is primarily linked to, and profoundly affected by, their structures that feature an S, N chelator [4,5]. In this regard, additional introduction of an N coordination site, such as α-pyridyl serves as an advantage as it forms a more stable N, N, S pincer-like chelation that results in more effective ion removal [7]. In this sense, TSCs are particularly effective for treating iron overload diseases such as leukemia and neuroblastoma [8]. Recently findings also suggested that, upon

 doi:10.20944/preprints202407.1597.v1

capturing of metal ions by TSCs, a different anticancer mechanism based on reactive oxygen species (ROS) chemistry can be commenced by taking advantage of the unique characteristics of the tumor microenvironment (TME), such as the overexpression of H_2O_2 and GSH [9–12]. The ROS generation can subsequently strengthen the chemotherapeutic outcome of TSCs.

The promising potential of TSCs as anticancer drugs has been manifested by several drugs that successfully entered clinical trials, such as 3-aminopyridine-2-carboxaldehyde thiosemicarbazone (Triapine), 5-hydroxypicolinaldehyde thiosemicarbazone (5-HP), and 4-(pyridine-2-yl)-N-([(8E)-5,6,7,8-tetrahydroquinolin-8-ylidene]amino)piperazine-1-carbothioamide (COTI-2) (Chart 1). Nevertheless, numerous side effects were also associated with these drugs, i.e., the formation of methemoglobin hypoxia by Triapine[13], severe hematological and gastrointestinal side effects for 5-HP[14], and drug resistance and other adverse effects (i.e., nausea, vomiting, and fatigue) for COTI-2 [15,16].

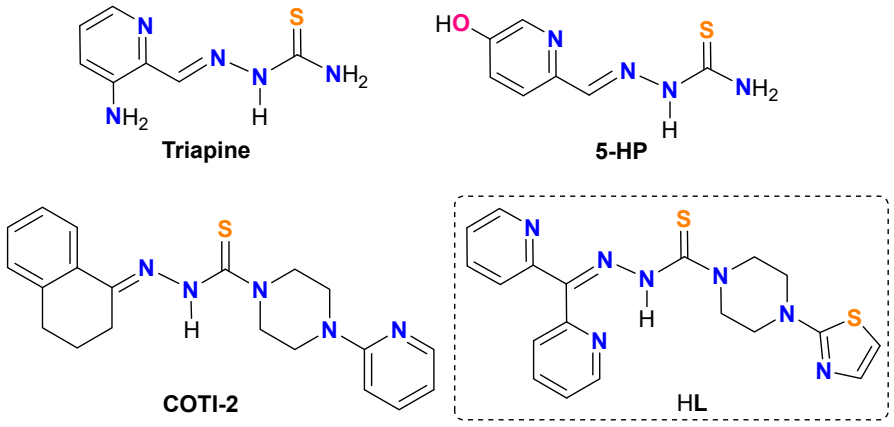

Chart 1. Molecular diagrams of Triapine, 5-HP, COTI-2, and H**L**.

In this work, we report the synthesis of a novel TSC-based anticancer drug of N′-(di(pyridin-2-yl)methylene)-4-(thiazol-2-yl)piperazine-1-carbothiohydrazide (H**L**) featuring di-2-pyridylketone for chelating-bridging and a thiazole spectator (Chart 1). Ligand H**L** can readily associate Cu^{2+} to give the corresponding coordination complexes of $[CuCl(\mathbf{L})]_2$ (**1**), and $[Cu(NO_3)(\mathbf{L})]_2$ (**2**). The structures of H**L**, **1**, and **2** were confirmed by various spectroscopic techniques and ultimately authenticated by single-crystal X-ray diffraction studies. **HL, 1, and 2 are highly toxic against hepatocellular carcinoma cell lines Hep-G2, PLC/PRF/5, and HuH-7. Notably, these species are extremely toxic for PLC/PRF/5, with the corresponding** half maximal inhibitory concentration (IC_{50}) **values as low as** 3.26 nmol/mL **(HL)**, 2.18 nmol/mL **(1)**, and 2.54×10^{-5} nmol/mL **(2). Our preliminary** pharmacokinetic studies of H**L** further revealed that oral administration (per os, PO) exhibits a significantly longer half-life $t_{1/2}$ of 21.61 ± 9.4 h as compared to that of the intravenous (i.v.) administration of 11.88 ± 1.66 h. These results highlight that H**L** and its relevant functional coordination complexes can be promising chemotherapeutic drugs for oral administration.

2. Results and Discussion

2.1. Synthesis and X-ray Structure Characterization of HL, $[CuCl(L)]_2$ (1), and $[Cu(NO_3)(L)]_2$ (2)

The synthesis of ligand H**L** was achieved by a five-step protocol to give an overall yield of 9.3% (Scheme 1). The purity of H**L** was confirmed by microanalysis, ^1H, and ^{13}C nuclear magnetic resonance (NMR) spectroscopy (Figure S1). The assumed connectivity of H**L** was also unambiguously determined by single-crystal X-ray diffraction studies (Figure 1a).

Preprints.org (www.preprints.org) | NOT PEER-REVIEWED | Posted: 19 July 2024 doi:10.20944/preprints202407.1597.v1

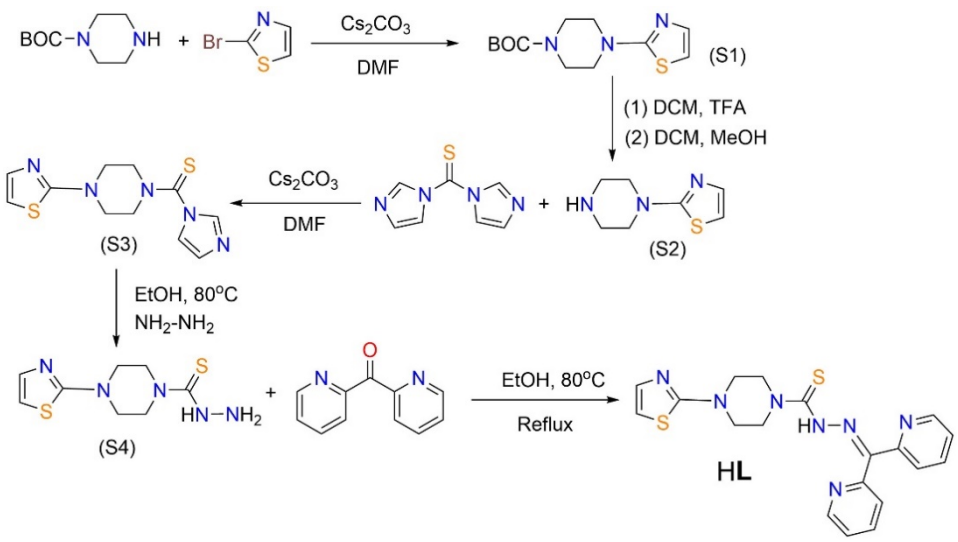

Scheme 1. The five-step synthetic procedure for H**L**.

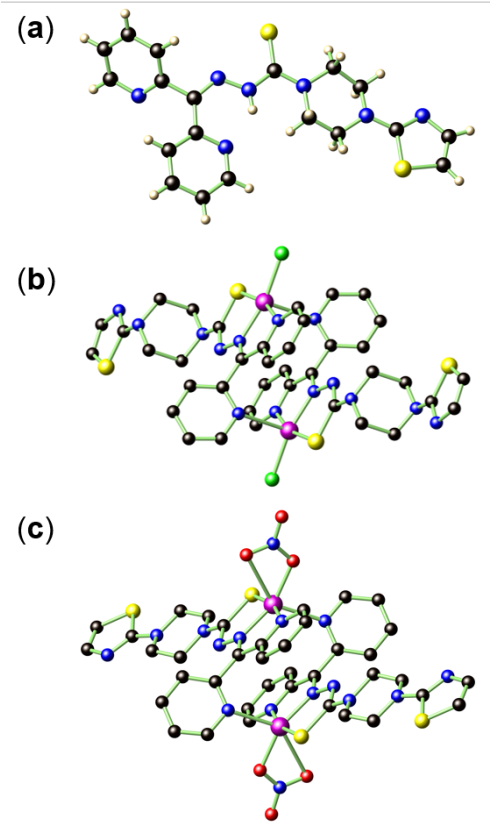

Figure 1. The single crystal structure of H**L** (a), **1** (b), and **2** (c). In (b) and (c), the H atoms were also omitted for clarity. Color legend: Cu dark magenta, Cl green, S yellow, O red, N blue, C black, H light pink.

Coordination complexes of **1** and **2** were prepared accordingly by reacting H**L** and the respective Cu(II) sources under appropriate conditions (Scheme 2). Single crystal X-ray structure data for **1** (Figure 1b) and **2** (Figure 1c) indicated that both compounds form dimeric structures in the solid state, enabled by the head-to-tail complementary Cu–N coordination. In **1**, each Cu^{2+} shows a square pyramidal coordination geometry, fulfilled by an S, one azomethinic N, one α-pyridyl N atom from an **L** ligand, and one Cl^- that defines the square plane, in addition to one pyridyl N atom from adjacent **L** ligand that occupies the apical position. A similar connectivity is also found in **2** except

 doi:10.20944/preprints202407.1597.v1

that one Cl^- is replaced by a chelating NO_3^-, yielding a distorted octahedral coordination geometry for Cu^{2+}.

Notably, the ligands in both **1** and **2** undergo a change of conjugation with the loss of hydrazinic proton and the conversion of C=S into C–S bond. Such structure variation is seen in a variety of transition metal complexes of α-pyridyl thiosemicarbazone chelators, such as Triapine complexes of Fe^{3+}/Ga^{3+}[17,18], di-2-pyridyl ketone 4,4-dimethyl-3-thiosemicarbazone (HDp44mT) complexes of Fe^{3+}[19], as well as several Cu^{2+} complexes [20]. Bormio Nunes et al. also reported that, for Fe^{3+}/Cu^{2+} complexes of COTI-2, the N–N single bond of the ligand is inherited in the final chelating complexes [16]. As a result of the C=S to C–S bond variation, the C=S bond distance in H**L** of 1.681(5) Å increased to 1.739(4) Å in **1** and 1.744(6) Å in **2** (Table S1). Nevertheless, the N–N distance in H**L** of 1.354(5) Å remained nearly unaltered as compared to the N=N distances in **1** (1.354(4) Å) and **2** (1.351(6) Å) due to the additional coordination of one N to Cu^{2+}.

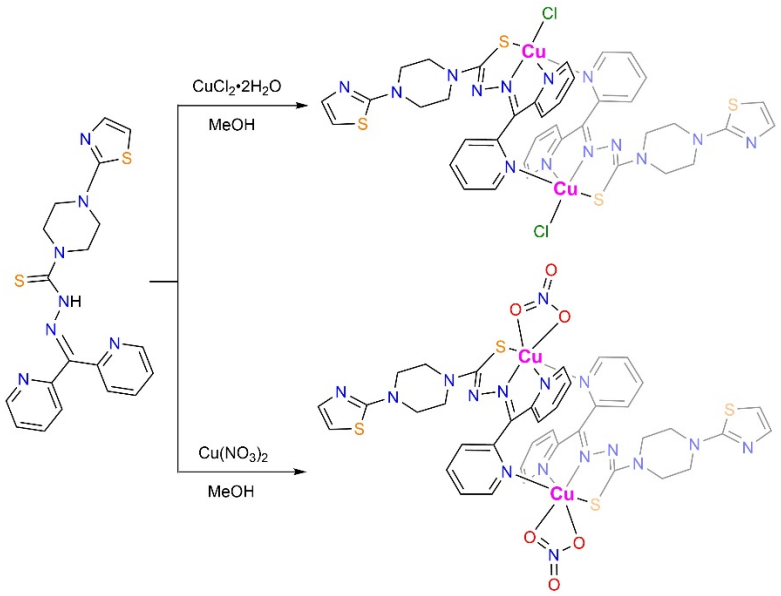

Scheme 2. The synthetic procedure for **1** and **2** from H**L**.

2.2. Spectroscopic Characterizations of HL, 1, and 2

Energy dispersive X-ray spectroscopy (EDS) revealed an atomic ratio of Cu : Cl : S of 2.0 : 2.2 : 4.2 in **1** and Cu : S of 2.0 : 4.6 in **2** (Figure S2), consistent with the derived ratio of Cu : Cl : S of 1.0 : 1.0 : 2.0 (**1**) and Cu : S of 1.0 : 2.0 (**2**) from single-crystal data, and the elements Cu, S, N and C are evenly distributed in their elemental mapping diagrams (Figure S2). The Fourier-transform infrared (FT-IR) spectra show that upon coordination with Cu^{2+}, the C=N bond vibration peaked at 1571 cm^{-1} in H**L** shifts to 1593 cm^{-1} for both **1** and **2** (Figure S3). Meanwhile, bands at 850 cm^{-1} (**1**) and 856 cm^{-1} (**2**) which were assignable as C=S bond vibrations, also shifted as compared to that of H**L** (869 cm^{-1}) upon bonding with Cu^{2+} [21,22]. In the ultraviolet-visible (UV-Vis) spectroscopy (Figure 2), ligand-to-metal charge transfer (LMCT) bands in **1** and **2** are found at 426 nm as compared to H**L** [23]. Meanwhile, the ligand-centered UV-Vis absorption band of the H**L** undergoes a significant blue shift due to the conjugation change and charge transfer reactions. The LMCT leads to the partial reduction of Cu^{2+} which is favorable for Cu^+-induced reactions, such as the ROS generation via the Fenton-like process [24]. The Cu 2p X-ray photoelectron spectroscopy (XPS) of both **1** and **2** revealed two sets of binding energies (Figure 3). Peaks at 933.8/953.5 eV (**1**) and 933.8/953.8 eV (**2**) are assignable as the spin-orbit splitting of Cu $2p_{3/2}$ and $2p_{1/2}$ of Cu^{2+} [25–27]. Two satellite peaks at 943.3/963.3 eV (**1**) and 943.4/963.0 eV (**2**) are also attributed to Cu^{2+} ions due to its d^9 electronic configuration that is susceptible to photoreduction to give a more stable d^{10} configuration.

Preprints.org (www.preprints.org) | NOT PEER-REVIEWED | Posted: 19 July 2024 doi:10.20944/preprints202407.1597.v1

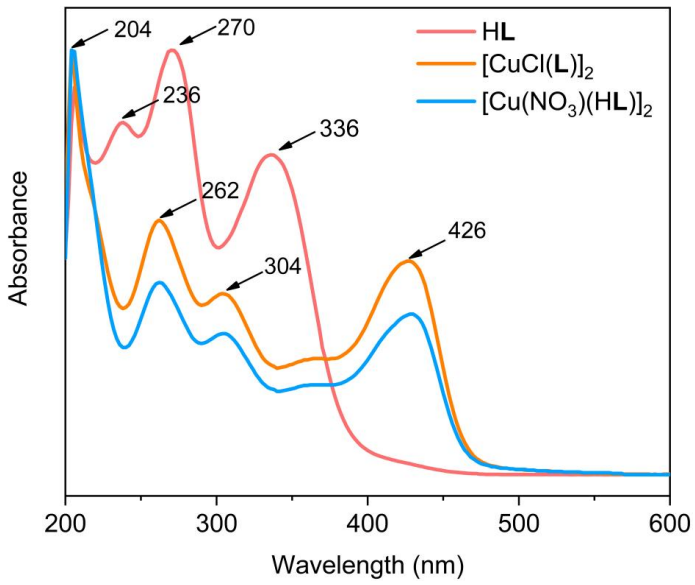

Figure 2. The UV-Vis spectra of H**L** (light red), **1** (light orange), and **2** (light blue) in MeOH solutions.

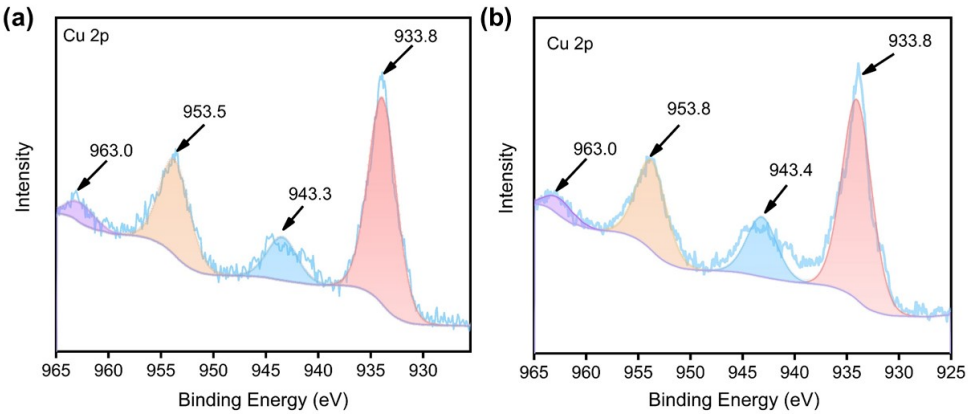

Figure 3. The Cu 2p XPS spectra of **1** (a) and **2** (b).

2.3. Hydroxyl Radical (•OH) Production

The generation of •OH from H_2O_2 by H**L**, **1**, and **2** was assayed by 3,3′,5,5′-tetramethylbenzidine (TMB) [12,28,29]. The colorless TMB can be quickly oxidized by •OH to give a characteristic blue charge-transfer complex oxTMB with intense absorption at 652 nm [30,31]. Different concentrations of H**L** (5, 10, 20, 30 μg/mL) or **1** and **2** containing equivalent H**L** were treated with (TMB) solution containing 100 μM H_2O_2, which is assumed as approximately the concentration reported to be present in tumor cells, or five times that in normal cells [32,33]. After 20 min of incubation with H**L**, there is no oxTMB found as suggested by both the UV-Vis and the direct observation of solution colors (Figure S4). In sharp contrast, both **1** and **2** can induce the generation of •OH under otherwise identical conditions in a concentration-dependent manner with **2** further outperforms **1** (Figure 4, and Figure S4). In addition, the MeOH solutions of H**L**, **1**, and **2** at H**L** / **L** concentrations of 30 μg/mL remained stable upon keeping for 72 h (Figure S5), as evidenced by their unaltered UV-Vis absorption patterns throughout the experiments.

 doi:10.20944/preprints202407.1597.v1

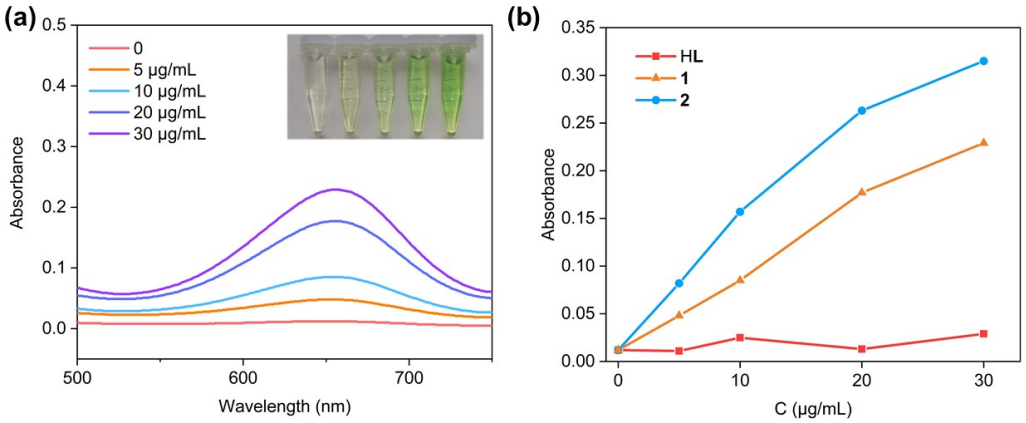

Figure 4. Change of UV-Vis absorption intensity in the range of 500–750 nm upon treatment with different concentrations of **1** in the presence of 100 μM H_2O_2 (a; inset: photographs showing color change upon introducing gradient concentrations of **1**). The intensity change at 652 nm (oxTMB) upon treating gradient concentrations of H**L**, **1**, and **2** with 100 μM H_2O_2 (b).

2.4. CCK-8 Assay for HL, 1, and 2

The cytotoxicity of H**L**, **1**, and **2** against three hepatocellular carcinoma cell lines Hep-G2, PLC/PRF/5, and HuH-7 were evaluated by cell counting kit-8 (CCK-8) assay. As shown in Figure 5, all three complexes demonstrate superior cytotoxicity originating from the ligand, particularly for the PLC/PRF/5 cell line. Notably, **1** and **2** demonstrated higher cytotoxicity as compared to the H**L**, presumably due to the additional ROS generation induced by the overexpressed H_2O_2 in the cancer cells. The IC_{50} values for H**L**, **1**, and **2** against PLC/PRF/5 were as low as 3.26 nmol/mL, 2.18 nmol/mL, and 2.54×10^{-5} nmol/mL, which is favorably lower than those against Hep-G2 (78.83 nmol/mL for H**L**, 38.11 nmol/mL for **1**, and 16.86 nmol/mL for **2**), and HuH-7 (192.20 nmol/mL for H**L**, 176.60 nmol/mL for **1**, and 87.53 nmol/mL for **2**) cell lines (Table S2).

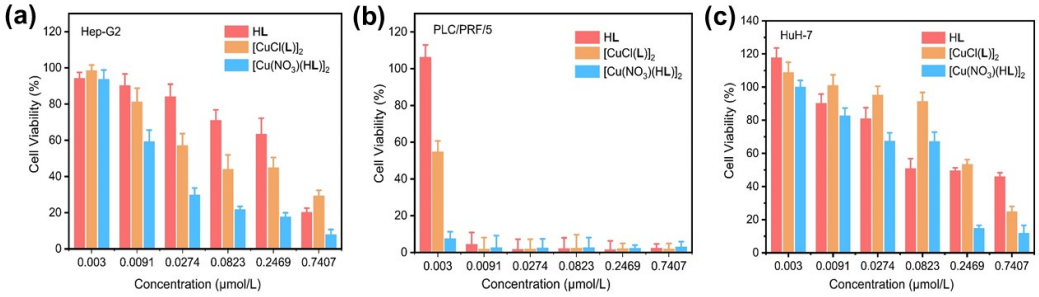

Figure 5. The viability of Hep-G2 (a), PLC/PRF/5 (b), and HuH-7 (c) cells when treated with gradient concentrations of H**L**, **1**, and **2** (n = 3).

2.5. Intracellular ROS Generation by HL, 1, and 2

Given the efficient •OH production in water induced by **1** and **2**, we next investigated in vitro ROS generation by **1** and **2** in the representative HuH-7 cell line using 2′,7′-dichlorodihydrofluorescein diacetate (DCFH-DA) as a fluorescence probe, and compared to that of H**L** [34,35]. The non-emissive DCFH-DA can readily be uptaken by the cell, where it is hydrolyzed into 2,7-dichlorodihydrofluorescein (DCFH) by cellular enzymes. Upon oxidation by ROS, DCFH can convert to 2,7-dichlorofluorescein (DCF) which gives bright green fluorescence [29,36]. As shown in Figure 6, H**L** alone produced negligible ROS. In sharp contrast, **1** and **2** can induce the formation of strong fluorescence characterizing the effective generation of ROS in the HuH-7 cells.

 doi:10.20944/preprints202407.1597.v1

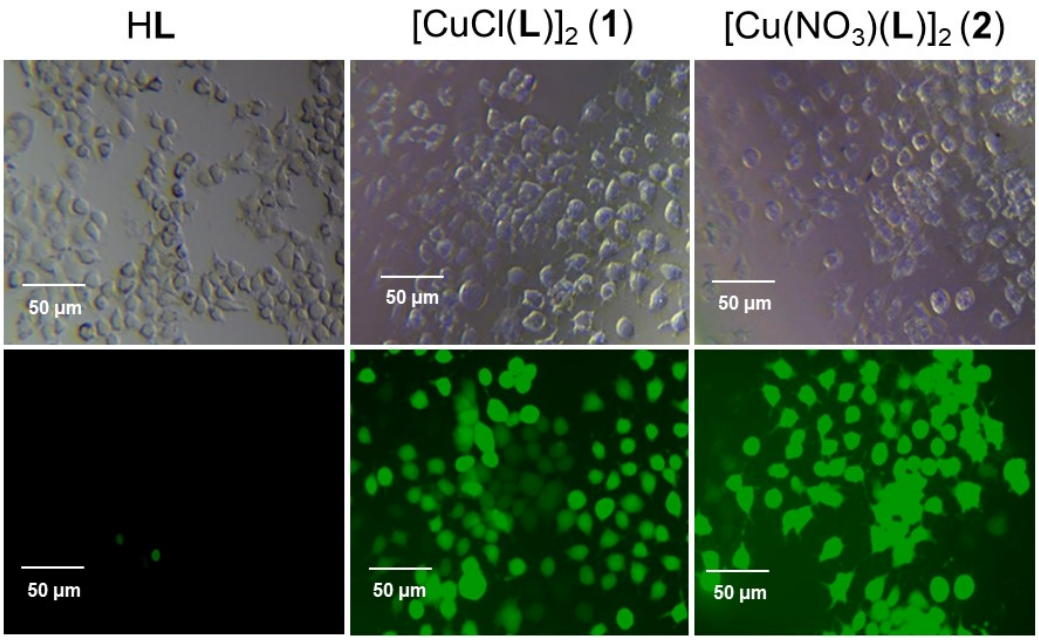

Figure 6. Comparison of the intracellular ROS generating ability of H**L**, **1**, and **2** in HuH-7 using DCFH-DA as a fluorescence probe.

2.6. In Vivo Pharmacokinetic Study of HL.

For pharmacokinetic studies, CD®(SD) IGS Rats (5−6 weeks old) were randomly divided into two groups (3 for each group) for oral administration (per os, PO) or intravenous administration (i.v.) of H**L** with dosages of 30 mg kg^{-1} and 0.5 mg kg^{-1}, respectively (Tables S4 and S5). The blood was then collected from the orbital sinus with a heparinized syringe at different time intervals (0.5, 1.0, 2.0, 4.0, 8.0, and 24 h for PO, and 0.03, 0.5, 1.0, 2.0, 4.0, 8.0, and 24 h for i.v.). High-performance liquid chromatography (HPLC) gives the mean area under the curve ($AUC_{0\text{-}inf}$) values of 10409.01 ± 5313.4 ng h mL^{-1} for PO, and 5701.36 ± 2647.15 ng h mL^{-1} for i.v. H**L** achieved the largest C_{max} value of 425.93 ± 176.1 ng mL^{-1} at a T_{max} of 1.0 h for PO, while for i.v., the C_{max} value of 806.43 ± 46.66 ng mL^{-1} was immediately observed at T_{max} of 0.03 h, which is expected for i.v. administration. Notably, the PO administration exhibits a significantly longer half-life $t_{1/2}$ of 21.61 ± 9.4 h, nearly doubled as compared to that of the i.v. administration of 11.88 ± 1.66 h (Figure 7), certifying that H**L** has a favorable pharmacokinetic via PO administration.

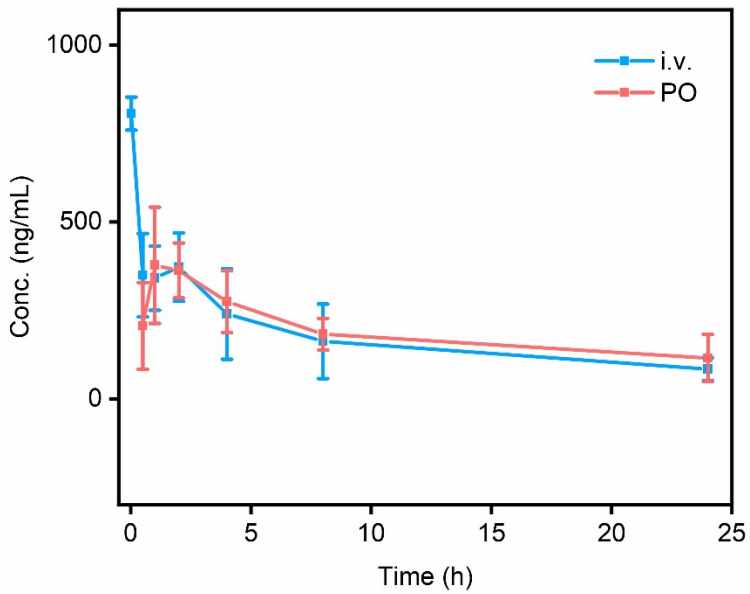

 doi:10.20944/preprints202407.1597.v1

Figure 7. The time-concentration relationships of H**L** via i.v. (0.5 mg kg^{-1}) and PO (30 mg kg^{-1}) administrations.

3. Materials and Methods

3.1. General

tert-Butyl piperazine-1-carboxylate (BOC-PIP; ≥99%, Aladdin), 2-bromothiazole (98%, Crgent Biotech), di-2-pyridyl ketone (98%, Crgent Biotech), NH_2NH_2 (≥95%, adamas), $Cu(NO_3)_2$ (≥99%, Aladdin), CuO (≥97%, Aladdin), DMF (≥99%, Aladdin), CH_2Cl_2 (≥99%, Aladdin), trifluoroacetic acid (TFA; ≥99%, Aladdin), i-PrOH (≥99%, Aladdin), methyl *tert*-butyl ether (MTBE, ≥99%, Aladdin), $NaHCO_3$ (>99%, Crgent Biotech), EtOH (≥95%), and Cs_2CO_3 (≥99%, Crgent Biotech) were commercially available and used without further purifications.

Hep-G2, and PLC/PRF/5, and HuH-7 cell lines were purchased from the Shanghai Institute of Cell Biology, Chinese Academy of Sciences. Phosphate buffer solution (PBS) was purchased from Shanghai Basal Media Technologies Co., Ltd. Cell culturing medium MEM (with NEAA + 10% FBS + 1% P/S), MEM (with NEAA + 1% P/S), DMEM (10% FBS + 1% P/S), McCoy's 5A (10% FBS + 1% P/S), DMEM (1% P/S), and 0.25% trypsin solution (containing EDTA, dissolved in PBS) were purchased from Procell Life Science & Technology Co., Ltd. The cell counting kit-8 (CCK-8) and the reactive oxygen species detection kit were from APEXBIO and Shanghai Beyotime Biotechnology Co., Ltd., respectively.

^{1}H nuclear magnetic resonance (NMR) spectra were obtained on a Varian UNITY plus-400/plus-600 NMR spectrometer (Varian, Inc., Palo Alto, CA, USA). Fourier transform infrared (FT-IR) spectra were measured on a Bruker VERTEX 70+HYPERION 2000 FT-IR spectrometer (Bruker AXS GmbH, Germany) using the attenuated total refraction (ATR) technique. Elemental analyses for C, H, and N were measured on a Carlo-Erba CHNO-S microanalyzer (Carlo Erba, Waltham, MA, USA). Ultraviolet-visible (UV-Vis) spectroscopy was obtained on a Varian Cary-50 UV-visible spectrophotometer (Varian, Inc., Palo Alto, CA, USA). X-ray photoelectron spectroscopy (XPS) was performed on an EXCALAB 250 XI X-ray photoelectron spectrometer (Thermo Scientific, Waltham, MA, USA). The high performance liquid chromatography (HPLC) were carried out on an Angilient 1260 Infinity II Bio-SEC system (Agilent Technologies, Inc., CA, USA). The CCK-8 cytotoxicity assay was conducted on a multifunction microplate detector by recording the absorption at 450 nm using a TECAN M1000PRO microplate reader (Tecan, Zürich, Switzerland).

3.2. Synthetic Steps for HL

Ligand H**L** can be synthesized via a five-step process as indicated below.

Step 1. Synthesis of S1. *t*-Butyloxy carbonyl (BOC) protected piperazine (BOC-PIP; 400.0 mg, 2.148 mmol) and 2-bromothiazole (529.0 mg, 3.221 mmol) were dissolved in DMF (4 mL) and stirred for 5 min. Cs_2CO_3 (1400 mg, 4.295 mmol) was added as a solid and the mixture heated overnight at 120°C. The formed product was extracted from H_2O using ethyl acetate to obtain S1 as a white solid. Yield (290 mg, 50% based on BOC-PIP). ^{1}H NMR (400 MHz, $CDCl_3$) δ 7.209 (s, 1H), 6.605 (s, 1H), 3.566 (s, 4H), 3.466 (s,4H), 1.483 (s, 9H). ^{13}C NMR (101 MHz, $CDCl_3$) δ 172.096, 154.601, 139.567, 107.814, 80.273, 48.456, 28.396.

Step 2. Synthesis of S2. Compound S1 (290.0 mg, 1.078 mmol) was dissolved in CH_2Cl_2 (4 mL) to obtain a light yellow-brown solution and trifluoroacetic acid (TFA, 12 mL) was subsequently added, and the solution quickly turned yellow upon stirring. The mixture was stirred for 2 h and the solvent evaporated, DCM / MeOH = 2 : 1 and $NaHCO_3$ were consequently introduced to obtain S2 as a light yellow powder. Yield (180 mg, 99% based on S1). ^{1}H NMR (400 MHz, DMSO-d_6) δ 9.845 (s, 1H), 7.360 (s, 1H), 7.088 (s, 1H), 5.039 (s, 7H), 3.843 (s, 4H), 3.257 (s, 4H). ^{13}C NMR (101 MHz, DMSO-d_6) δ 170.534, 133.871, 110.024, 46.268, 41.908.

Step 3. Synthesis of S3. Complex S2 (180.0 mg, 1.065 mmol) was added to CH_2Cl_2 (5 mL) to form a suspension, and Cs_2CO_3 (342.0 mg, 1.917 mmol) was introduced to give a yellow solution. The mixture was stirred at r.t. for 15 h, and the product was washed with H_2O and extracted with CH_2Cl_2.

 doi:10.20944/preprints202407.1597.v1

The organic layers were combined and dried. The pure yellow compound of S3 can be isolated by chromatography using CH_2Cl_2/i-PrOH (25 : 1, v/v) as the eluent. Yield (270 mg, 91% based on S2). ^{1}H NMR (400 MHz, $CDCl_3$) δ 7.904 (s, 1H), 7.234 (s, 2H), 7.111 (s, 1H), 6.683 (s, 1H), 4.040 (s, 4H), 3.656 (s, 4H). ^{13}C NMR (101 MHz, $CDCl_3$) δ 179.348, 170.996, 139.720, 137.427, 130.303, 119.252, 108.941, 50.694, 48.032.

Step 4. Synthesis of S4. Compound S3 (270.0 mg, 0.968 mmol) was added to EtOH (4 mL) to form a suspension, and NH_2NH_2 (0.0063 mL, excess) was subsequently added. The mixture was heated to reflux at 80°C to yield a white suspension of S4 which was purified by chromatography using CH_2Cl_2/MeOH (25 : 1, v/v) as the eluent. Yield (175 mg, 74% based on S3). ^{1}H NMR (400 MHz, DMSO-d_6) δ 9.225 (s, 1H), 7.189 (s, 1H), 6.881 (s, 1H), 4.802 (s, 2H), 3.882 (s, 4H), 3.417 (s, 4H). ^{13}C NMR (101 MHz, DMSO-d_6) δ 183.080, 171.525, 139.917, 108.901, 48.052, 46.913.

Step 5. Synthesis of H**L**. Compound S4 (40.0 mg, 0.165 mmol) was dissolved in EtOH (10 mL) and stirred for 10 min. Di-2-pyridyl ketone (34.0 mg, 0.181 mmol) was subsequently introduced and the mixture was heated to reflux at 80°C overnight. Upon cooling to r.t., the crude powder of H**L** was recrystallized with MeOH / MTBE (5 : 1, v/v) to give a pure product of yellow-green solid of H**L**. Yield (18.8 mg, 28% based on S4). Single crystals of H**L** were grown by slow evaporation of a MeOH/DMSO (v/v = 1 : 1) solution of H**L**. Anal. Calcd for $C_{19}H_{19}N_7S_2$: C 55.72, H 4.68, N 23.94; found: C 55.26; H 4.93; N, 23.49. IR (ATR, cm^{-1}): 3053(w), 2842(w), 1572(m), 1519(vs), 1487(s), 1464(s), 1382(s), 1339(m), 1305(vs), 1279(vs), 1220(vs), 1204(vs), 1130(vs), 1104(s), 1048(s), 1016(vs), 995(vs), 962(s), 916(s), 898(w), 870(m), 858(w), 802(vs), 785(s), 762(m), 743(vs), 723(vs), 693(vs), 669(m), 656(m), 642(s), 618(s). ^{1}H NMR (400 MHz, DMSO-d_6) δ 14.64 (s, 1H), 8.89 (s, 1H), 8.61 (s, 1H), 7.98 (s, 3H), 7.60 (s, 3H), 7.20 (s, 1H), 6.89 (s, 1H), 4.16 (s, 4H), 3.32 (s, 4H). ^{13}C NMR (101 MHz, DMSO-d_6) δ 170.77, 148.40, 147.95, 139.47, 137.79, 137.30, 126.84, 124.64, 123.78, 108.38, 48.33, 47.45.

3.3. Synthesis and Characterization of $[CuCl(L)]_2$ (1)

Method 1: H**L** (100 mg, 0.244 mmol) was introduced in 20 mL MeOH to give a yellow suspension, and $CuCl_2 \bullet 2H_2O$ (42 mg, 0.246 mmol) in 10 mL MeOH was subsequently introduced dropwise. The formed mixture was stirred at 40°C for 8 h. The solvent was removed, and the formed brown powder was recrystallized in MeOH and Et_2O to obtain the crystal of **1**.

Method 2: CuO (21.4 mg, 0.269 mmol) and HCl (19.6 mg, 0.537 mmol) were mixed in 3 mL of MeOH and the mixture stirred at 40°C. With the gradual dissolution of CuO, the solution turned pale green. After 10 min, H**L** (100 mg, 0.244 mmol) was introduced and the solution became dark brown. The mixture was stirred for an additional 2 h and then filtered, washed with a mixture of MeOH/MTBE (1 : 1, v/v; MTBE = methyl tert-butyl ether) to give a brown powder of $[CuCl(\mathbf{L})]_2$ which was dried under vacuo. Yield (220 mg, 89% based on H**L**). Anal. Calcd for $C_{38}H_{40}Cl_2Cu_2N_{14}S_4$: C 44.79, H 3.96, N 19.24; found: C 44.18, H 3.37, N 18.96. IR (ATR, cm^{-1}): 3077(w), 2993(w), 2645(w), 1592(s), 1563(m), 1476(w), 1458(w), 1440(vs), 1418(s), 1383(s), 1364(vs), 1318(w), 1289(m), 1275(s), 1247(vs), 1193(m), 1169(w), 1130(s), 1089(w), 1058(w), 1012(s), 982(w), 966(w), 956(w), 923(s), 850(m), 812(m), 795(s), 772(w), 738(m), 709(m), 686(w), 664(s), 644(s), 612(m).

3.4. Synthesis and Characterization of $[Cu(NO_3)(L)]_2$ (2)

$Cu(NO_3)_2$ (50.5 mg, 0.269 mmol) and H**L** (100 mg, 0.244 mmol) were mixed in 3 mL MeOH and the mixture was stirred at 40°C to obtain a dark brown solution, and upon further stirring for 2 h, the solution turned dark green. The mixture was filtered and washed with a mixture of MeOH/MTBE (1 : 1, v/v; MTBE = methyl tert-butyl ether) to give a brown powder of **2** which was dried under vacuo. Single crystals were obtained by slow diffusion of Et_2O into a MeOH solution of **2**. Yield (235 mg, 90% based on H**L**). Anal. Calcd for $C_{38}H_{36}Cu_2N_{16}O_6S_4$: C 42.73, H 3.40, N 20.98; found: C 42.38, H 3.33, N 20.81. IR (ATR, cm^{-1}): 3080(w), 2846(w), 1592(m), 1520(s), 1483(s), 1461(vs), 1424(vs), 1380(s), 1338(w), 1278(vs), 1239(vs), 1203(vs), 1140(vs), 1102(m), 1052(w), 1012(vs), 920(s), 897(w), 855(m), 819(m), 792(s), 744(m), 724(w), 700(m), 665(m), 615(m).

 doi:10.20944/preprints202407.1597.v1

3.5. Single Crystal X-ray Crystallography

Diffraction data for H**L**, **1**, and **2** were acquired either on a Bruker APEX II CCD X-ray diffractometer (Bruker AXS GmbH, Germany) using Mo-Kα (λ = 0.71073 Å) (H**L**) or Ga-Kα (λ = 1.34138 Å) irradiation (**1** and **2**). Refinement and reduction of the collected data were achieved using the program Bruker SAINT and absorption corrections were performed using a multi-scan method [37]. All the crystal structures were solved by direct methods and refined on F^2 by full-matrix least-squares techniques with SHELXTL-2016 [38]. Crystallographic data for H**L**, **1**, and **2** have been deposited in the Cambridge Crystallographic Data Center (CCDC) as supplementary publication numbers 2341904 (H**L**), 2341905 (**1**), and 2341906 (**2**). These data can be obtained free of charge either from the CCDC via www.ccdc.cam.ac.uk/data_request/cif or from the Supporting Information. A summary of the key crystallographic data for H**L**, **1**, and **2** is listed in Table 1. Selected bond distances and angles were listed in Table S1.

Table 1. A summary of the cell parameters and refinement results for H**L**, **1**, and **2**.

	HL	**[CuCl(L)]$_2$ (1)**	**[Cu(NO$_3$)(L)]$_2$ (2)**
CCDC number	2341904	2341905	2341906
Formula	$C_{19}H_{19}N_7S_2$	$C_{38}H_{40}Cl_2Cu_2N_{14}S_4$	$C_{38}H_{36}Cu_2N_{16}O_6S_4$
Formula weight	409.53	1019.06	1068.15
Crystal system	Triclinic	Triclinic	Monoclinic
Space group	*P*-1	*P*-1	$P2_1/n$
a/Å	10.4251(14)	9.342(2)	10.7226(16)
b/Å	10.7193(14)	10.714(2)	9.6646(15)
c/Å	11.0200(15)	11.378(3)	21.695(3)
α/°	105.347(5)	93.542(10)	90
β/°	103.115(5)	109.660(10)	104.187(2)
γ/°	117.474(5)	108.609(9)	90
V/Å^3	962.0(2)	998.0(4)	2179.7(6)
Z	2	1	2
D_c/(g cm^{-3})	1.414	1.696	1.627
F(000)	428	522	1092
μ /mm^{-1}	0.298	8.151	1.235
Total reflns.	25863	16310	33191
Uniq. reflns.	3928	4037	4404
Observed reflns.	1855	3572	3194
Parameters	253	274	298
R_{int}	0.1570	0.0818	0.0905
R^a	0.0882	0.0592	0.0677
wR^b	0.1738	0.1658	0.1470
GOF^c	1.029	1.079	1.048

$^a R = \Sigma||F_o|-|F_c||/\Sigma|F_o|$. $^b wR = \{\Sigma w(F_o^2-F_c^2)^2/\Sigma w(F_o^2)^2\}^{1/2}$. $^c GOF = \{\Sigma w((F_o^2-F_c^2)^2)]/(n-p)\}^{1/2}$, where n = number of reflections and p = total number of parameters refined.

3.6. In Vitro Cytotoxicity Evaluation by CCK-8 Assay

The HuH-7 cell line was cultured in DMEM + 10% FBS + 1% P/S and DMEM + 1% P/S. Cells grew as a monolayer and were detached upon confluence using trypsin (0.5% w/v in PBS). The cells were harvested from the cell culture medium by incubating in trypsin solution for 3 min, and then centrifuged with the supernatant subsequently discarded. 3 mL portion of serum-supplemented cell culture medium was added to neutralize any residual trypsin. The cells were re-suspended in serum-supplemented DMEM at a concentration of 5 × 10^4 cells/mL. Cells were cultured at 37°C and 5% CO_2 for the CCK-8 studies. HuH-7 cells were seeded at a density of 2 × 10^4 cells per well in 90 µL of culture medium (DMEM + 10% FBS + 1% P/S), and cultured for 24 h at 37°C and 5% CO_2 for attachment. The

 doi:10.20944/preprints202407.1597.v1

culture medium was then replaced by a serum-free medium (DMEM + 1% P/S) containing various concentrations of H**L**, **1**, and **2** (Pharmaceuticals solubilized with 2 parts per thousand DMSO). All experiments were carried out with three replicates (n = 3), and the untreated cells served as the 100% cell viability control, while the cell-free medium (DMEM + 10% FBS + 1% P/S + CCK-8) served as the blank. HuH-7 cells were directly incubated for a period of 72 h. After incubation, 100 μL of culture medium (DMEM + 10% FBS + 1% P/S) and 10 μL CCK-8 was introduced and cultured for an additional 2 h before spectrophotometric measurement at 450 nm on a microplate reader. The relative cell viability (%) related to control cells was calculated using the equation:

$$V\% = \frac{[A]_{experimental} - [A]_{blank}}{[A]_{control} - [A]_{blank}} \times 100\%$$

in which V% is the percentage of cell viability, $[A]_{experimental}$ is the absorbance of the wells culturing the treated cells, $[A]_{blank}$ is the absorbance of the blank, and $[A]_{control}$ is the absorbance of the wells culturing untreated cells. The cytotoxicity assessment for Hep-G2 and PLC/PRF/5 resembled that of HuH-7 except that the culturing media was different, viz MEM (NEAA) + 10% FBS + 1% P/S and MEM (NEAA) + 1% P/S for both Hep-G2 and PLC/PRF/5.

3.7. Detection of Intracellular Reactive Oxygen Species

HuH-7 cells were introduced into a 12-well plate (4×10^5 per well) in 1 mL of growing media (DMEM + 10% FBS + 1% P/S) and the cells were incubated at 37°C under 5% CO_2 for 24 h for attachment. The growing media was removed and the wells were replenished with H**L**, **1**, and **2** in 1 mL growing media (with 2 ppm of DMSO) with equivalent H**L** concentrations of 2 μg/mL. The cells were incubated for an additional 2 h and then the culturing media was replaced with 10 μmol/mL DCFH-DA in DMEM + 1% P/S (1 mL), prepared by diluting (1 : 1000) a concentrated DCFH-DA following the supplied protocols. The cells were incubated for a further 20 min and then the culturing media was removed. The cells were further rinsed with culturing media (DMEM + 1% P/S) three times to remove the residual DCFH-DA, and observed under a BD5000 inverted microscope to estimate and compare the ROS generation abilities of these materials.

3.8. Pharmacokinetics of HL

CD®(SD) IGS Rats (5−6 weeks old) were purchased from Beijing Vital River Laboratory Animal Technology Co., Ltd. All animal experiments were used in accordance with the requirements of the Experimental Animal Welfare Ethics Committee of Transcenta Diagnostic Technology (Suzhou) Co., LTD (PZ-20211210001). For pharmacokinetic experiments, SD rats were randomly divided into two groups, with 3 for PO administration (30 mg kg^{-1}) and i.v. administration (0.5 mg kg^{-1}), respectively. Plasma was collected from the jugular vein with the presence of a heparinized syringe at different time intervals, viz. 0.5, 1.0, 2.0, 4.0, 8.0, and 24 h for PO, and 0.03, 0.5, 1.0, 2.0, 4.0, 8.0, and 24 h for i.v. Plasma was first centrifuged at 3500 rpm for 10 min, then 0.05mL of the plasma was extracted, then trifluoroacetic acid was used to acid precipitate protein, and NaOH to neutralize the solution. The mixture was diluted using MeCN: H_2O (5 : 5 v/v). After 10 min of precipitating, supernatant fluids were collected by centrifugation at 10000 rpm for 5 min and filtered with a syringe through a 0.22 μm hydrophilic membrane filter and measured by HPLC method. For the HPLC assay, the analytical column was an Agilent ZORBAX SB C_{18} column (4.6 mm × 150 mm, 5 μm. The mobile phase was MeCN: H_2O (5:5 v/v), the flow rate of the mobile phase was 0.8 mL min^{-1} and the UV detector was at 245 nm.

4. Conclusions

In this work, we report that the thiosemicarbazone derivative of H**L** and its Cu(II) complexes **1** and **2** demonstrated superior anticancer performances against hepatocellular carcinoma cell lines Hep-G2, PLC/PRF/5, and HuH-7. For **1** and **2**, the involvement of ROS as catalyzed by the Fenton-like process is also obvious. Intriguingly, the pharmacokinetic studies revealed that H**L** can be successfully absorbed via PO administration, with a favorable half-life of 21.61 ± 9.4 h, almost double

 doi:10.20944/preprints202407.1597.v1

that of via i.v. administration, rendering HL promising clinical potential. We believe that the association of such type of ligand with diverse metal ions may further equip the drug with additional beneficial features, such as the modulation of acute toxicity, toxicity via ROS, and on-demand metal supplements during the curation process.

Supplementary Materials: The following supporting information can be downloaded at the website of this paper posted on Preprints.org, additional figures and tables.

Author Contributions: Conceptualization, W.H.Z. and G.Y.; methodology, S.Y.L. and C.M.Z.; software, W.H.Z. and C.M.Z.; validation, C.M.Z., P.X., W.H.Z. and G.Y.; formal analysis, S.Y.L. C.M.Z., and P.X.; data curation, Y.N. and M.L.D.; writing—original draft preparation, S.Y.L. and C.M.Z.; writing—review and editing, W.H.Z., and G.Y.; supervision, W.H.Z.; project administration, W.H.Z. and G.Y.; funding acquisition, W.H.Z. All authors have read and agreed to the published version of the manuscript.

Funding: We are grateful to SuZhou LongMab Biosciences., Ltd. for the final support of this work.

Conflicts of Interest: The authors declare no conflict of interest.

References

1. Klayman, D.L.; Scovill, J.P.; Bartosevich, J.F.; Mason, C.J. 2-Acetylpyridine thiosemicarbazones. 2. N^4,N^4-Disubstituted derivatives as potential antimalarial agents. *J. Med. Chem.* **1979**, *22*, 1367−1373.
2. Beraldo, H.; Gambinob, D. The wide pharmacological versatility of semicarbazones, thiosemicarbazones and their metal complexes. *Mini. Rev. Med. Chem.* **2004**, *4*, 31−39.
3. Kalinowski, D.S.; Quach, P.; Richardson, D.R. Thiosemicarbazones: The new wave in cancer treatment. *Future Med. Chem.* **2009**, *1*, 1143−1151.
4. Shakya, B.; Yadav, N.P. Thiosemicarbazones as potent anticancer agents and their modes of action. *Mini. Rev. Med. Chem.* **2020**, *20*, 638−661.
5. Serda, M.; Kalinowski, D.S.; Rasko, N.; Potůčková, E.; Mrozek-Wilczkiewicz, A.; Musiol, R.; Małecki, J.G.; Sajewicz, M.; Ratuszna, A.; Muchowicz, A., et al. Exploring the anti-cancer activity of novel thiosemicarbazones generated through the combination of retro-fragments: Dissection of critical structure-activity relationships. *Plos One* **2014**, *9*, e110291.
6. Dilworth, J.R.; Hueting, R. Metal complexes of thiosemicarbazones for imaging and therapy. *Inorg. Chim. Acta* **2012**, *389*, 3−15.
7. Yuan, J.; Lovejoy, D.B.; Richardson, D.R. Novel di-2-pyridyl–derived iron chelators with marked and selective antitumor activity: In vitro and in vivo assessment. *Blood* **2004**, *104*, 1450−1458.
8. Richardson, D.R. Iron chelators as therapeutic agents for the treatment of cancer. *Crit. Rev. Oncol. Hematol.* **2002**, *42*, 267−281.
9. Guo, Y.; Hu, P.; Shi, J. Nanomedicine remodels tumor microenvironment for solid tumor immunotherapy. *J. Am. Chem. Soc.* **2024**, *146*, 10217−10233.
10. Whiteside, T.L. The tumor microenvironment and its role in promoting tumor growth. *Oncogene* **2008**, *27*, 5904−5912.
11. Zou, Y.-M.; Li, R.-T.; Yu, L.; Huang, T.; Peng, J.; Meng, W.; Sun, B.; Zhang, W.-H.; Jiang, Z.-H.; Chen, J., et al. Reprogramming of the tumor microenvironment using a PCN-224@IrNCs/d-Arg nanoplatform for the synergistic PDT, NO, and radiosensitization therapy of breast cancer and improving anti-tumor immunity. *Nanoscale* **2023**, *15*, 10715−10729.
12. Hou, Y.-K.; Zhang, Z.-J.; Li, R.-T.; Peng, J.; Chen, S.-Y.; Yue, Y.-R.; Zhang, W.-H.; Sun, B.; Chen, J.-X.; Zhou, Q. Remodeling the tumor microenvironment with core–shell nanosensitizer featuring dual-modal imaging and multimodal therapy for breast cancer. *ACS Appl. Mater. Interfaces* **2023**, *15*, 2602−2616.
13. Ma, B.; Goh, B.C.; Tan, E.H.; Lam, K.C.; Soo, R.; Leong, S.S.; Wang, L.Z.; Mo, F.; Chan, A.T.C.; Zee, B., et al. A multicenter phase II trial of 3-aminopyridine-2-carboxaldehyde thiosemicarbazone (3-AP, Triapine®) and gemcitabine in advanced non-small-cell lung cancer with pharmacokinetic evaluation using peripheral blood mononuclear cells. *Invest. New Drugs* **2008**, *26*, 169−173.
14. DeConti, R.C.; Toftness, B.R.; Agrawal, K.C.; Tomchick, R.; Mead, J.A.R.; Bertino, J.R.; Sartorelli, A.C.; Creasey, W.A. Clinical and pharmacological studies with 5-hydroxy-2-formylpyridine thiosemicarbazone. *Cancer Res.* **1972**, *32*, 1455−1462.
15. Westin, S.N.; Nieves-Neira, W.; Lynam, C.; Salim, K.Y.; Silva, A.D.; Ho, R.T.; Mills, G.B.; Coleman, R.L.; Janku, F.; Matei, D. Abstract CT033: Safety and early efficacy signals for COTI-2, an orally available small molecule targeting p53, in a phase I trial of recurrent gynecologic cancer. *Cancer Res.* **2018**, *78*, CT033−CT033.
16. Bormio Nunes, J.H.; Hager, S.; Mathuber, M.; Pósa, V.; Roller, A.; Enyedy, É.A.; Stefanelli, A.; Berger, W.; Keppler, B.K.; Heffeter, P., et al. Cancer cell resistance against the clinically investigated thiosemicarbazone

COTI-2 is based on formation of intracellular copper complex glutathione adducts and ABCC1-mediated efflux. *J. Med. Chem.* **2020**, *63*, 13719−13732.

17. Kowol, C.R.; Trondl, R.; Heffeter, P.; Arion, V.B.; Jakupec, M.A.; Roller, A.; Galanski, M.S.; Berger, W.; Keppler, B.K. Impact of metal coordination on cytotoxicity of 3-aminopyridine-2-carboxaldehyde thiosemicarbazone (triapine) and novel insights into terminal dimethylation. *J. Med. Chem.* **2009**, *52*, 5032−5043.
18. Kowol, C.R.; Berger, R.; Eichinger, R.; Roller, A.; Jakupec, M.A.; Schmidt, P.P.; Arion, V.B.; Keppler, B.K. Gallium(III) and iron(III) complexes of α-N-heterocyclic thiosemicarbazones: Synthesis, characterization, cytotoxicity, and interaction with ribonucleotide reductase. *J. Med. Chem.* **2007**, *50*, 1254−1265.
19. Richardson, D.R.; Sharpe, P.C.; Lovejoy, D.B.; Senaratne, D.; Kalinowski, D.S.; Islam, M.; Bernhardt, P.V. Dipyridyl thiosemicarbazone chelators with potent and selective antitumor activity form iron complexes with redox activity. *J. Med. Chem.* **2006**, *49*, 6510−6521.
20. Bai, X.-G.; Zheng, Y.; Qi, J. Advances in thiosemicarbazone metal complexes as anti-lung cancer agents. *Front. Pharmacol.* **2022**, *13*, 1018951.
21. Quiroga, A.G.; M. Pérez, J.; López-Solera, I.; Montero, E.I.; Masaguer, J.R.; Alonso, C.; Navarro-Ranninger, C. Binuclear chloro-bridged palladated and platinated complexes derived from *p*-isopropylbenzaldehyde thiosemicarbazone with cytotoxicity against cisplatin resistant tumor cell lines. *J. Inorg. Biochem.* **1998**, *69*, 275−281.
22. Souza, R.A.C.; Costa, W.R.P.; de F. Faria, E.; Bessa, M.A.d.S.; Menezes, R.d.; Martins, C.H.G.; Maia, P.I.S.; Deflon, V.M.; Oliveira, C.G. Copper(II) complexes based on thiosemicarbazone ligand: Preparation, crystal structure, Hirshfeld surface, energy framework, antiMycobacterium activity, in silico and molecular docking studies. *J. Inorg. Biochem.* **2021**, *223*, 111543.
23. Carcelli, M.; Tegoni, M.; Bartoli, J.; Marzano, C.; Pelosi, G.; Salvalaio, M.; Rogolino, D.; Gandin, V. In vitro and in vivo anticancer activity of tridentate thiosemicarbazone copper complexes: Unravelling an unexplored pharmacological target. *Eur. J. Med. Chem.* **2020**, *194*, 112266.
24. Juliá, F. Ligand-to-metal charge transfer (LMCT) photochemistry at 3d-metal complexes: An emerging tool for sustainable organic synthesis. *ChemCatChem* **2022**, *14*, e202200916.
25. Cui, Y.; Ding, Y.; Molina, S.E.V.; Li, Y. A mixed-valence Cu^{II}/Cu^{I} coordination polymer based on bridged thiocyanate and in situ formed di(N-heterocyclic) sulfide: Synthesis, structure, and magnetic properties. *J. Mol. Struct.* **2021**, *1241*, 130623.
26. Meda, L.; Ranghino, G.; Moretti, G.; Cerofolini, G.F. XPS detection of some redox phenomena in Cu-zeolites. *Surf. Interface Anal.* **2002**, *33*, 516−521.
27. Zeng, C.-M.; Luo, S.-Y.; Wang, X.; Cao, F.-L.; Zhang, Z.-S.; Zhang, W.-H.; Dai, C.-L.; Young, D.J. A porphyrin-based 3D metal-organic framework featuring $[Cu_8Cl_6]^{10+}$ cluster secondary building units: Synthesis, structure elucidation, anion exchange, and peroxidase-like activity. *Chem. Asian J.* **2024**, *19*, e202400237.
28. Hu, J.-J.; Yu, X.-Z.; Zhang, S.-Q.; Zhang, Y.-X.; Chen, X.-L.; Long, Z.-J.; Hu, H.-Z.; Xie, D.-H.; Zhang, W.-H.; Chen, J.-X., et al. Hydrogel with ROS scavenging effect encapsulates BR@Zn-BTB nanoparticles for accelerating diabetic mice wound healing via multimodal therapy. *iScience* **2023**, *26*, 106775.
29. Li, Q.; Xu, B.-W.; Zou, Y.-M.; Niu, R.-J.; Chen, J.-X.; Zhang, W.-H.; Young, D.J. Nanoscale two-dimensional Fe^{II}- and Co^{II}-based metal−organic frameworks of porphyrin ligand for the photodynamic therapy of breast cancer. *Molecules* **2023**, *28*, 2125.
30. Josephy, P.D.; Eling, T.; Mason, R.P. The horseradish peroxidase-catalyzed oxidation of 3,5,3′,5′-tetramethylbenzidine. Free radical and charge-transfer complex intermediates. *J. Biol. Chem.* **1982**, *257*, 3669−3675.
31. Yuan, B.; Chou, H.-L.; Peng, Y.-K. Disclosing the origin of transition metal oxides as peroxidase (and catalase) mimetics. *ACS Appl. Mater. Interfaces* **2022**, *14*, 22728−22736.
32. Chu, Z.; Yang, J.; Zheng, W.; Sun, J.; Wang, W.; Qian, H. Recent advances on modulation of H_2O_2 in tumor microenvironment for enhanced cancer therapeutic efficacy. *Coord. Chem. Rev.* **2023**, *481*, 215049.
33. Wang, Y.; Gao, F.; Li, X.; Niu, G.; Yang, Y.; Li, H.; Jiang, Y. Tumor microenvironment-responsive Fenton nanocatalysts for intensified anticancer treatment. *J. Nanobiotechnology* **2022**, *20*, 69.
34. Wang, X.; Feng, J.-H.; Zeng, C.-M.; Zhang, Z.-S.; Cao, F.-L.; Zhang, W.-H.; Chen, J.-X.; Young, D.J. $[Fe^{III}Cl(TMPPH_2)][Fe^{III}Cl_4]_2$: A stand-alone molecular nanomedicine that induces high cytotoxicity by ferroptosis. *Molecules* **2024**, *29*, 2495.
35. Huang, N.; Tang, X.-Y.; Meng, W.; Lai, Y.-H.; Zhou, X.; Yu, X.-Z.; Zhang, W.-H.; Chen, J.-X. Immunogenic radiation therapy for enhanced antitumor immunity via a core–shell nanosensitizer-mediated immunosuppressive tumor microenvironment modulation. *ACS Nano* **2023**, *17*, 19853−19864.
36. Li, W.; Li, R.; Ye, Q.; Zou, Y.; Lu, X.; Zhang, W.; Chen, J.; Zhao, Y. Mn_3O_4 nanoshell coated metal–organic frameworks with microenvironment-driven O_2 production and GSH exhaustion ability for enhanced chemodynamic and photodynamic cancer therapies. *Adv. Healthc. Mater.* **2023**, *12*, 2202280.

 doi:10.20944/preprints202407.1597.v1

37. Sheldrick, G.M. SADABS (Version 2.03): Program for empirical absorption correction of area detector data; University of Göttingen, Germany. **1996**.
38. Sheldrick, G.M. Crystal structure refinement with SHELXL. *Acta Crystallogr., Sect. C* **2015**, *71*, 3–8.